Local indirect magnetoelectric coupling at twin walls in $CaMnO_3$

Ida C. Skogvoll,* Benjamin A. D. Williamson, and Sverre M. Selbach†
Department of Materials Science and Engineering, Faculty of Natural Sciences and Technology, NTNU Norwegian University of Science and Technology, NO-7491 Trondheim, Norway

(Received 18 November 2025; revised 13 March 2026; accepted 1 May 2026; published 1 June 2026)

Ferroelastic twin walls in centrosymmetric perovskites can host emergent polar and magnetic properties forbidden in the bulk. We use density functional theory calculations to study the geometry and magnetic properties of ferroelastic domain walls in orthorhombic $CaMnO_3$, which belongs to the most common perovskite space group, *Pnma*. At the wall, the inherent inversion symmetry breaking induces local polar distortions dependent on the wall geometry, which couple to the magnetic order through the octahedral distortions. Noncollinear calculations reveal enhanced out-of-plane magnetic moments on the Mn atoms and a local, finite magnetization confined to the wall. Strain fields across twin walls thus give rise to coexistence of polarization and magnetization as well as magnetoelectric response that is absent and symmetry forbidden in bulk $CaMnO_3$. We propose that magnetoelectric coupling and coexisting polarization and magnetization can emerge at twin walls in bulk centrosymmetric antiferromagnets.

DOI: 10.1103/6y99-279q

I. INTRODUCTION

Multiferroics are a class of materials that simultaneously exhibit at least two ferroic orders, and where the coexistence of magnetic order and ferroelectricity plays a particularly prominent role. The coupling of these orders is central to the development of multifunctional devices, where, for instance, the magnetization or polarization direction can be switched by an applied electric or magnetic field [1]. However, the existence of ferroelectric and magnetic order parameters does not necessarily entail a strong coupling between the two. On the contrary, the common microscopic origins responsible for ferroelectric and magnetic orders are mutually exclusive by nature, and in the rare case that they do coexist, they are usually only weakly related [2].

Considerable efforts have been put into finding nondisruptive coupling mechanisms between the distortion mode responsible for polarization and the magnetic order. A notable contribution is improper ferroelectrics where the polar displacement results from complex spin structures that break inversion symmetry [3]. Nonetheless, as frustrated magnetism commonly only features at very low temperatures and ferromagnetism is often achieved through double exchange, materials that exhibit a coupling between polarization and ferromagnetism are exceedingly rare [4–6]. Other proposals consist of materials-by-design strategies for engineering weak ferromagnetism, where symmetry considerations are used to construct specific criteria for the interplay of spin and lattice degrees of freedom [7–9]. Both of these mechanisms are rooted in the Dzyaloshinskii-Moriya interaction (DMI), a relativistic correction to superexchange coupling, favoring noncollinear spin ordering [10,11].

A class of materials that lend themselves well to engineering multiferroics are the perovskite oxides. They have highly tunable properties deriving from the connection between structural, chemical, and spin degrees of freedom, as well as susceptibility of the ABO_3 structure to compositional engineering [12–15]. Importantly, there is a prominent coupling between the characteristic rotations of the oxygen octahedra and the magnetic order in transition metal perovskites. Such rotational distortions in simple perovskites do not break inversion symmetry, and thus cannot contribute to a magnetoelectric coupling. However, in some layered perovskites a switchable magnetization by polarization reversal has been found, caused by a DMI and polar distortion emerging from the same octahedral distortion [9,16,17].

Because of their abundance, ferroelastic materials provide ample opportunities for investigating the relationship between magnetic order and octahedral rotations. Materials that exhibit either ferroelectricity or magnetism along with ferroelasticity are often not designated as being multiferroic, due to their less obvious technological potential. Hence, magnetism in ferroelastic materials has received less attention than in ferroelectrics. Nevertheless, in ferroelastic domain walls, inversion symmetry is inherently broken, and they exhibit an emergent strain field stabilizing a local metastable structure. As the order parameter switches from one domain to the other, the domain wall structure approaches a local symmetry that is distinctly different from the bulk, enabling functional properties that are not found within each domain [18].

$CaMnO_3$ has the orthorhombic *Pnma* symmetry in its ground state with a complex domain wall structure. This structure is characterized by the out-of-phase rotations of

*Contact author: ida.c.skogvoll@ntnu.no
†Contact author: selbach@ntnu.no

Published by the American Physical Society under the terms of the Creative Commons Attribution 4.0 International license. Further distribution of this work must maintain attribution to the author(s) and the published article's title, journal citation, and DOI.

successive MnO_6 octahedra around two of the pseudocubic axes and in-phase rotations around the remaining axis, corresponding to an $a^-a^-c^+$ Glazer tilt notation, where the three letters each represent an axis along with the tilting magnitude and phase ("+" being in phase and "−" being out of phase). This leads to a $\sqrt{2}a_c \times \sqrt{2}a_c \times 2a_c$ expansion of the unit cell with respect to the high-temperature cubic phase. Like many ABO_3 structures, it has a polar instability in the B-site cation, suppressed by the primary antiferrodistortive order parameter. This can be activated by straining the material, for example, through antiphase boundaries or twin walls [19–21]. Previous attempts to achieve ferroelectricity in the *Pnma* phase have involved epitaxially straining thin films and building superlattices with mismatched layer constituents [22–24]. Straining $CaMnO_3$ can also induce other functionalities such as defect-formation control [25,26]. The space group of $CaMnO_3$ allows canted antiferromagnetic order [27,28], where the size of the canting is related to the octahedral rotations as well as the strength of the DMI and superexchange interactions [29]. In other words, the bonding environment set by the octahedral rotation angles strongly affects the magnetic order through spin-phonon coupling [30]. However, the magnetic order of $CaMnO_3$ does not allow for a magnetoelectric response [31].

The coexistence of collinear magnetic and polar orders at ferroelastic domain walls has been explored previously in terms of substitutional doping with magnetic ions [32] and in undoped $CaMnO_3$ [33]. Here, we show that the intrinsic symmetry breaking in two types of ferroelastic domain walls in $CaMnO_3$ can facilitate a local net polarization and magnetization and that these order parameters are coupled. The larger octahedral distortions at twin walls favor parallel spins compared to the bulk antiferromagnetism. Our results also reveal that the polarization profile and the amplitude of the net polar distortion are largely contingent on the specific magnetic configuration. Thus, the broken inversion symmetry indirectly lifts the suppression of the magnetoelectric effect in the sense that the polarization couples to the magnetization through the primary order parameter. Noncollinear calculations show that a larger canting is induced at the domain wall, providing a net enhancement of the out-of-plane magnetization.

The alteration of magnetic order at an interface has been treated in a few experimental and theoretical studies. However, these works involve superlattices, such as $LaAlO_3/PbTiO_3$ [34], or multiferroics with a vanishing polarization at the domain wall [35–37]. In $TbMnO_3$, uncompensated spins at nonpolar twin walls lead to a net in-plane magnetic moment [38]. Strain-mediated coupling between magnetic and polar orders in ferroelastic domain walls is thus proposed as a way to achieve a magnetoelectric response in single-phase perovskite oxides.

II. COMPUTATIONAL METHODS

DFT calculations were carried out using the VASP [39,40] code and the PBEsol functional [41] with a spin-polarized GGA + U implementation [42], to which a Hubbard U correction of 4 eV was applied to the Mn $3d$ orbitals [43]. The projector augmented wave [44] method was used, where Ca($3s^2, 3p^6, 4s^2$), Mn($3s^2, 3p^6, 3d^6, 4s^1$), and O($2s^2, 2p^4$) were treated as valence electrons. A plane-wave cutoff energy of 550 eV was applied, along with a Γ-centered $6 \times 6 \times 5$ k-point mesh for the primitive cell, with a corresponding k-point density employed for all other cell sizes. Atomic positions were relaxed until the residual forces were less than 0.001 eV/Å. Domain wall structures with $8 \times 1 \times 1$ supercells of 40-atom unit cells were relaxed to below 0.02 eV/Å. Phonon calculations were completed using the finite difference method implemented in the PHONOPY package, using $2 \times 2 \times 2$ and $3 \times 3 \times 3$ supercells for the 40-atom and primitive cells, respectively [45,46]. The ISOTROPY software suite was used for group-theoretical analysis [47]. Noncollinear magnetic calculations were conducted by including spin-orbit coupling self-consistently, both for determining the magnetocrystalline anisotropy energy and the magnetic wall (MW) configuration. A $6 \times 1 \times 1$ supercell with the converged domain wall geometry was constructed by removing the middle domain portions of the relaxed $8 \times 1 \times 1$ cell. VESTA was used for visualization and illustration of the crystal structures [48]. Relaxed structure files used in the calculations were uploaded to Zenodo [49].

TABLE I. Wyckoff position and coordinates of all sites in the optimized ground state structure for $CaMnO_3$.

Atom	Wyckoff position	x	y	z
Ca	4*c*	0.0076	0.0392	1/4
Mn	4*b*	1/2	0	0
O	4*c*	0.9290	0.4876	1/4
	8*d*	0.2893	0.2884	0.0370

III. RESULTS AND DISCUSSION

The optimized lattice constants a, b, and c of the ground state primitive cell were determined to be 5.231 Å, 5.267 Å, and 7.410 Å, respectively. These values are lower than reported work using PBE, but close to experimental values of 5.271 Å, 5.280 Å, and 7.457 Å [14]. For the remainder of this work, the convention of defining the c axis as the axis of in-phase rotations is used, corresponding to a *Pbnm* setting. Coordinates of all Wyckoff positions are presented in Table I. The ground state magnetic ordering is denoted G-AFM, where spins are antiparallel between all neighboring Mn atoms. The energies and geometric parameters associated with different collinear magnetic orders are presented in Table II, where it becomes apparent that in all cases parallel spins lead to a longer bond length and narrower bond angle, while antiparallel spins generate the opposite response. This is consistent with the parallel spin state favoring smaller orbital overlap, following the Goodenough-Kanamori-Anderson rules detailed in Sec. III 2. The C-AFM ordering, with parallel spins only in the c direction is closest to the ground state, and the ferromagnetic (FM) is the least favorable. While these results highlight the notable spin-phonon coupling between the magnetic order and the octahedral rotations, there is only a few degrees separating a spin parallel versus an antiparallel configuration.

TABLE II. Energy and geometric parameters for $CaMnO_3$ with different magnetic orderings in the primitive cell. The energy is calculated as the difference between the particular magnetic ordering and the G-AFM ground state. ϕ and α denote the angle and average bond lengths in the Mn-O-Mn bonds of the ab plane, while δ and β represent all Mn-O-Mn angles and bonds in the c direction (the axis of in-phase tilting).

	Energy (meV/u.c.)	Lattice parameters (Å)			Mn-O-Mn bond angles (deg)		Bond lengths (Å)	
	dE	a	b	c	ϕ	δ	α	β
G-AFM	0	5.231	5.267	7.410	155.8	157.0	1.898	1.891
C-AFM	18.07957	5.231	5.264	7.423	155.9	156.2	1.898	1.896
A-AFM	34.85726	5.232	5.284	7.406	154.9	157.1	1.905	1.889
FM	90.91948	5.236	5.286	7.422	154.7	155.8	1.907	1.898

Octahedral tilting is the most common type of structural distortion in the perovskite phase and can be defined in terms of the three-dimensional irreducible representations (irrep) M_3^+ and R_4^+ (using the convention where the B site is at the origin) of the high-symmetry $Pm\bar{3}m$ space group; see Fig. 1(a). Investigating the phonon spectrum of the cubic phase, these distortions manifest themselves as imaginary modes at the M and R points of the Brillouin zone, along with a zone-center mode (Γ_4^-) representing the polar displacement of the B-site cation [50]. Applying the polar distortion to the cubic structure leads to no further energy lowering. This is consistent with $CaMnO_3$ having a B-site polar instability suppressed by the emergence of octahedral rotations at the antiferrodistortive phase transition, which are common competing structural instabilities in the perovskite family [24,25,51,52]. Results from the phonon calculations are presented in Sec. I of the Supplemental Material [53]. As $CaMnO_3$ has an orthorhombic crystal structure, it is ferroelastic by construction. The expanded pseudocubic unit cell, as shown in Fig. 1(b), exhibits a twin angle (γ) related to the primitive a and b lattice parameters. This can be calculated as $\gamma = 90 - 2\tan^{-1}(a/b)$, amounting to a twin angle of 0.4°.

1. Ferroelastic domain wall structure

To establish the number of unique domain wall configurations, it is helpful to define the domain state in terms of the antipolar A-site distortion in the $\langle 110\rangle_{pc}$ directions; see Fig. 1(a). This X_5^+ mode is an improper order parameter, coupled to the M and R modes through a trilinear coupling term, $\alpha Q_R Q_M Q_X$, in the free energy expansion. Calculations demonstrating this improper mechanism can be found in Sec. I of the Supplemental Material [53]. The direction of the X-mode displacement is dictated by the local environment of octahedral rotations [55]. Defining each rotational mode as $R_x(a^-a^0c^0)$, $R_y(a^0a^-c^0)$, and $M_z(a^0a^0c^+)$, the trilinear term can be decoupled as

$$F = \alpha_1 Q_{R_x} Q_{M_z} Q_{X_x} + \alpha_2 Q_{R_y} Q_{M_z} Q_{X_y}, \quad (1)$$

where α_1 and α_2 are arbitrary coupling coefficients [56].

The shape of the unit cell, and therefore the strain state, is coupled to this A-site distortion such that modifying the ferroelastic domain state is associated with changing the sign of either Q_{X_x} or Q_{X_y}. Thus, switching from one ferroelastic domain to another involves reversing the tilting phase of either a single R mode or an R mode and M mode in combination. As a result, there are four different domain wall configurations which can be categorized by whether the interfacing domains

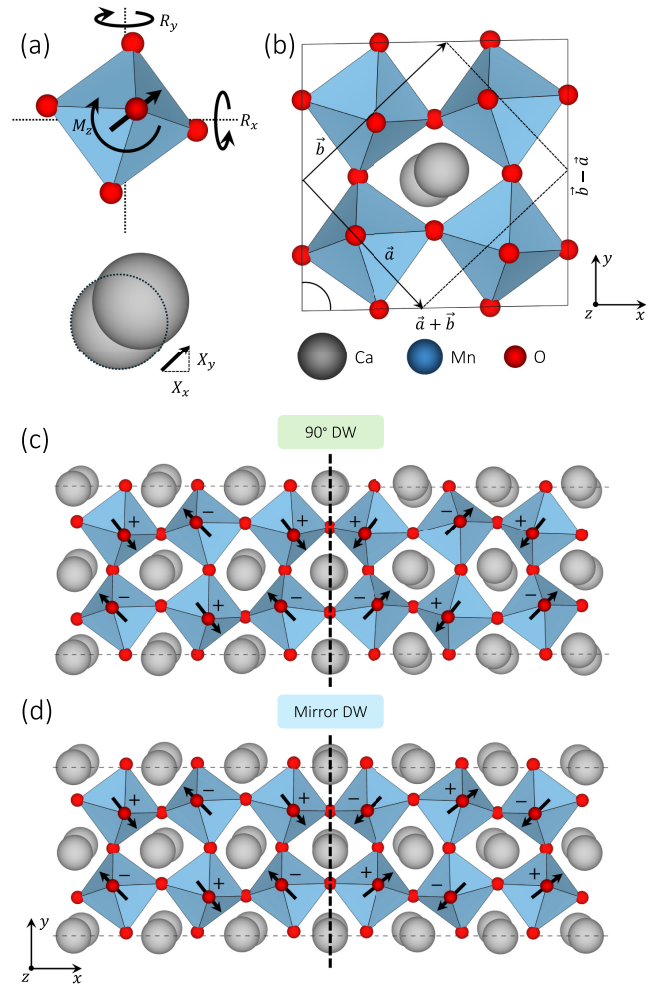


FIG. 1. (a) The distortion modes present in the ground state of $CaMnO_3$. The top octahedron illustrates the rotational modes around each pseudocubic axis, namely, the R_4^+ (here denoted R_x and R_y by their respective rotational axis) and M_3^+ (denoted M_z). The bottom figure displays the A-site displacement in the xy plane, decoupled as an X_y and X_x mode along each axis. (b) Dashed lines mark the orthorhombic primitive cell, while solid lines display the strained 40-atom cell. The arc at the lower left vertex indicates the angle $90° - \gamma$, where γ is the twin angle. (c), (d) Relaxed mirror and 90° ferroelastic domain wall cells. Black arrows show the octahedral tilting direction resulting from the out-of-phase rotations, and "+" and "–" denote a clockwise or counter-clockwise in-phase rotation around the z axis, prior to relaxation. The black dashed line illustrates the center position of the domain wall. Note that only half of the supercell is displayed here.

are related by a mirror plane or a 90° rotation around the z axis. Structures that lead to a disruption of the tilting pattern but no alteration of the strain direction result in structural antiphase boundaries [57]. These will not be considered further. For more details on the calculation of the different domain wall configurations, see Sec. II in the Supplemental Material [53].

For this work, one domain wall structure resulting from a 90° rotation and one exhibiting a mirror plane was constructed in the $(100)_{pc}$ plane. The former represents a switching of the R_x and M_z rotational modes, while the latter only switches the tilting phase of the first mode, covering the two kinds of tilting distortions expected at a ferroelastic wall. These walls will from here on be referred to as the 90° wall and mirror wall; see Figs. 1(c) and 1(d). The two walls in each supercell are structurally different interfaces although they have the same change in tilting phase. For each domain wall type, the domain wall formation energy was converged by testing dimensions $4 \times 1 \times 1$, $6 \times 1 \times 1$, and $8 \times 1 \times 1$, leading to values $E_{f,\mathrm{DW}(90^\circ)} = 163\,\mathrm{mJ}/m^2$ and $E_{f,\mathrm{DW(mirror)}} = 67\,\mathrm{mJ}/m^2$. The former value closely agrees with previous calculated values for similar 90° domain walls in $CaTiO_3$ [58]. The lower formation energy of the latter domain wall is a natural consequence of less strain across a mirror plane. These formation energies are significantly larger than for the twin walls in $SrTiO_3$ that are reported to be around $0.4\,\mathrm{mJ}/m^2$ [21]. However, the domain walls in $SrTiO_3$ separate $a^0a^0c^-$ and $a^0a^0(-c^-)$ domains that only require minor structural rearrangement across the boundary and thus a far more subtle local strain field. In contrast, the domain wall energies in $CaMnO_3$ are of similar magnitude to structural antiphase boundaries in $PbZrO_3$, reported to be $190\,\mathrm{mJ}/m^2$ [59], and domain walls in prototypical proper ferroelectrics like $LiNbO_3$ and $PbTiO_3$, with calculated energies of 120-160 mJ/m^2 [60] and $141 - 158\,\mathrm{mJ}/m^2$ [61].

Since the strain field across the domain wall stems from the phase change in the antiferrodistortive rotations of the oxygen octahedra, the primary order parameter Q can be defined as the decomposed angle of rotation about each of the unit cell directions, coinciding with the pseudocubic axes and the chains of MnO_6 octahedra. For each octahedron, the rotation is explicitly defined in terms of the angle of four Mn-O bonds in the corresponding plane normal to the rotation axis, relative to the Cartesian coordinate system (or pseudocubic axes). The average angle around the x axis is then defined as

$$\theta_x = \frac{1}{4}\sum_{\lambda=1}^{4} \sin^{-1}(\hat{\mathbf{r}}_{yz,\mathrm{CM}-O_\lambda} \times \hat{\mathbf{r}}'_{yz,\mathrm{CM}-O_\lambda}), \tag{2}$$

where $\hat{\mathbf{r}}_{yz}$ is the unit vector pointing from the center of mass (CM) of the oxygen octahedra to each of the O atoms within the yz plane, indexed by λ, projected into the same plane. $\hat{\mathbf{r}}'_{yz}$ is the equivalent unit vector in the cubic cell, which coincides with the Cartesian axes. If each position of an octahedron is indexed by the integers (i, j, k), the decomposed order parameter for each layer parallel to the domain wall can be defined as

$$Q_{R_x,R_y}(i) = \frac{1}{4}\sum_{j,k}(-1)^{j+k}\theta_{x,y}, \tag{3}$$

$$Q_{M_z}(i) = \frac{1}{4}\sum_{j}(-1)^{j}\theta_{z}, \tag{4}$$

where the phase of octahedral rotations is accounted for.

The resulting order parameter evolution throughout each supercell is displayed in Figs. 2(a) and 2(b). In both cases, one of the order parameters pass through zero, exhibiting a $\tanh(Q)$ relation, while the parameters that do not switch tilting phase follow a $\cosh(Q)$ profile, as expected from Landau theory [62]. The width of each domain wall was determined to be $w_{\mathrm{DW}(90^\circ)} = 19$ Å and $w_{\mathrm{DW(mirror)}} = 11$ Å. These results also fit well with the larger strain field expected for the 90° domain wall and the dissimilar formation energies. Similar thin domain walls are also found in other ferroelastic oxides with the *Pnma* structure [32].

The emergence of polar instabilities due to the vanishing of the primary order parameter is a well-known phenomenon and prevalent in ferroelastic domain walls [32]. The polarization originates from off-centering of the B-site ion. For $CaMnO_3$, the polarization profile is therefore calculated as the displacement (D) of the Mn atom from the CM of the encompassing oxygen octahedra; see Figs. 2(c) and 2(d). For a vanishing order parameter component, the ensuing polar distortion is of an antipolar character at each side of the domain wall, while for a nonvanishing and thus continuous tilting phase, a net polar distortion in one direction emerges. For the 90° domain wall, this results in a large antipolar distortion in the x direction and a net Mn displacement in the y direction. For the mirror domain wall, there is a similar profile for the y component, while also displaying a small net displacement in the z direction. The D_y component of the polar distortion switches directions at each domain wall within each supercell, meaning that it is locked to the local octahedral environment and thus of an improper nature. A detailed examination of the polarization profile in $CaTiO_3$ and $CaMnO_3$, both in terms of A-site and B-site distortions, is given in Ref. [33]. It is emphasized that the qualitative changes are different for each wall and that the magnitude of distortion is larger for the 90° domain wall. By determining the isotropy subgroups of each of the irreps M_3^+ and R_4^+, any possible evolution in the primary order parameter space is mapped out, thus listing potential switching pathways and intermediate domain wall symmetries; see Table III. It is challenging to identify a specific intermediate symmetry from the domain wall structure itself because it is too narrow to encompass a full unit cell. There is therefore a distinction between the extrapolated space group and the actual symmetry of the unit cell centered at the wall. However, listing all possible intermediate symmetries that do not lead to over-lapping in- and out-of-phase rotations around a single axis, all resulting space groups have inversion symmetry and are nonpolar. The 90° wall and mirror wall approximate a *Cmcm* and $P4_2/nmc$ symmetry, respectively. For the former domain wall, the loss of in-phase rotations entails a complete re-alignment of the antipolar A-site distortion, while for the latter there is only a re-alignment in the direction normal to the wall [the second term in Eq. (1) remains].

This group-theoretical analysis is inherently three-dimensional and does not account for gradient effects that result from the quasi-two-dimensional nature of a domain

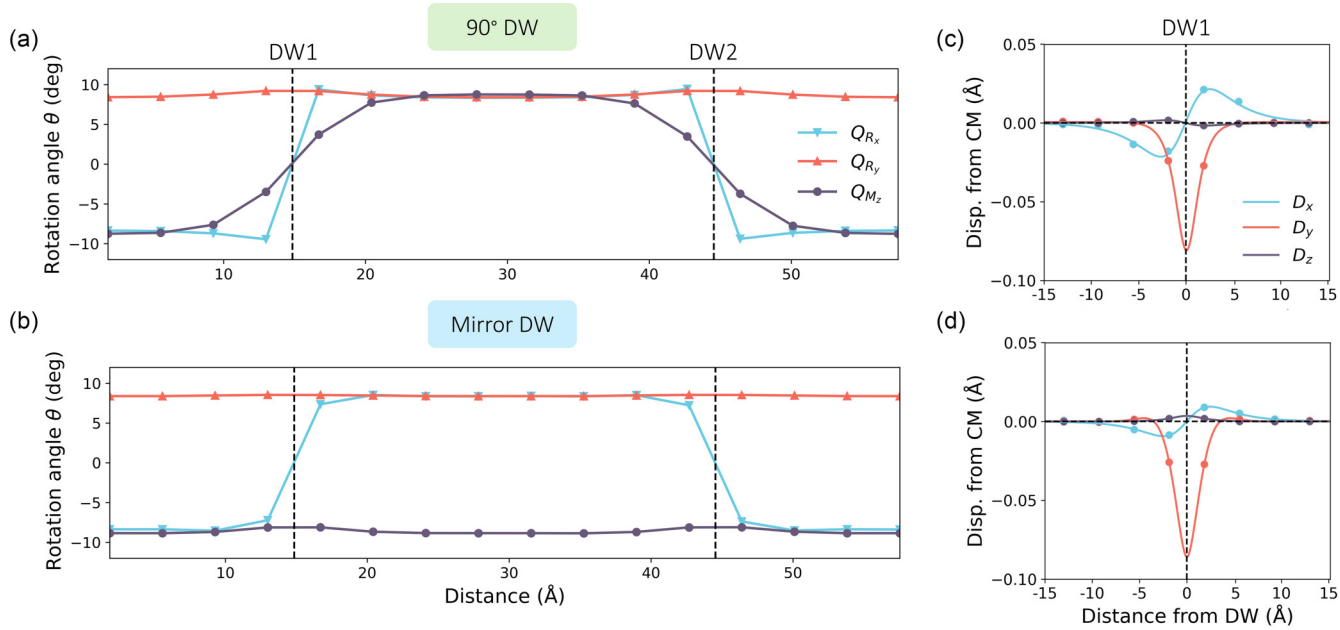


FIG. 2. (a), (b) Order parameter evolution calculated as the rotation angle around the x, y, and z axes, as a function of the distance through the domain wall cell for (a) a 90° wall and (b) a mirror wall. The location of each domain wall is indicated by the dashed lines. (c), (d) Polar distortion profiles of each domain wall type for the first domain wall of the cell, denoted DW1. The distortion is calculated as the displacement (D) of the Mn atom from the center of mass (CM) of the surrounding oxygen octahedron. DW2 shows the same trend, except that the direction of D_y is reversed. For the mirror wall, D_z is also reversed.

wall. However, it accentuates that additional distortions, in terms of A-site and B-site displacements, do not result from the symmetry pertaining to the primary order parameter, but is rather a secondary and purely flexoelectric effect. This is also in accordance with the larger polar distortion observed at the 90° domain wall, which also exhibits the larger structural deformation. This effect of spontaneous polarization is predicted for $CaTiO_3$ and other nonferroelectric perovskites to originate from the strain discontinuity at the boundary [63].

2. Magnetic domain walls

The magnetic order in $CaMnO_3$ is described by the superexchange formalism, where the exchange interaction occurs through an intermediary nonmagnetic atom, in this case the O atom connecting two Mn. The exact strength and sign of the exchange interaction is based on the specific symmetry relations of the bonding orbitals, their electron occupancy, and how strongly they overlap [64–66]. Spin ordering can thus be largely attributed to the Mn-O bond lengths and angles, embodied in the local octahedral environment [67]. In terms of

TABLE III. Isotropy subgroups of $Pm\bar{3}m$ generated from irreps M_3^+ and R_4^+ [50]. Only order parameter directions consistent with a well-defined Glazer notation is listed, i.e., where the order-parameter directions of each irrep is not overlapping in terms of crystal axes.

	Order parameter direction			
Irreps	M_3^+	R_4^+	Space group	Glazer notation
M_3^+	(a;0;0)		$P4/mbm$	$a^0a^0c^+$
	(a;a;0)		$I4/mmm$	$a^0b^+b^+$
	(a;a;a)		$Im\bar{3}$	$a^+a^+a^+$
	(a;b;c)		$Immm$	$a^+b^+c^+$
R_4^+		(a,0,0)	$I4/mcm$	$a^0a^0c^-$
		(a,a,0)	$Imma$	$a^0b^-b^-$
		(a,a,a)	$R\bar{3}c$	$a^-a^-a^-$
		(a,b,0)	$C2/m$	$a^0b^-c^-$
		(a,b,b)	$C2/c$	$a^-b^-b^-$
		(a,b,c)	$P\bar{1}$	$a^-b^-c^-$
$M_3^+ \oplus R_4^+$	(a;0;0)	(0,0,b)	$Cmcm$	$a^0b^-c^+$
	(a;0;0)	(0,b,b)	$Pnma$	$a^-a^-c^+$
	(a;0;0)	(0,b,c)	$P2_1/m$	$a^-b^-c^+$
	(a;a;0)	(0,0,b)	$P4_2/nmc$	$a^+a^+c^-$

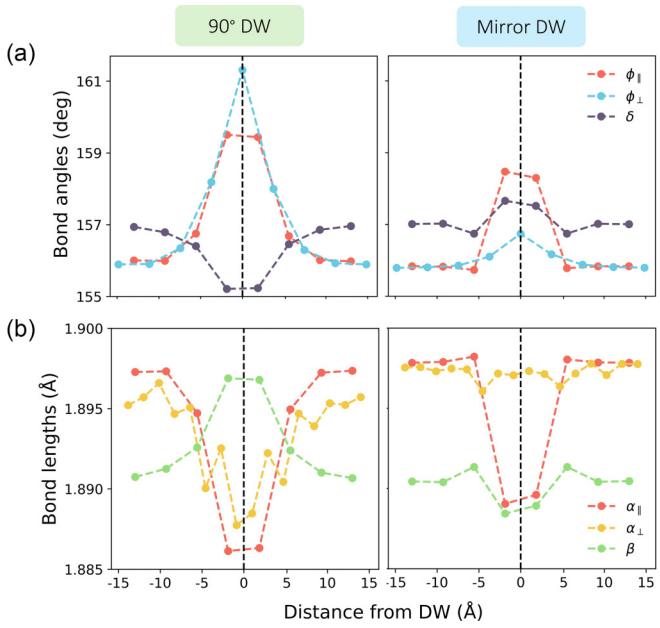


FIG. 3. (a) Average Mn-O-Mn bond angles calculated as a function of distance from the first domain wall in each supercell. δ represents the angles around the axis of in-phase rotations (z), while $\phi_\parallel$ and $\phi_\perp$ are the in-plane angles, parallel and perpendicular to the domain wall. (b) Bond length alteration at each domain wall. $\alpha_\parallel$ and $\alpha_\perp$ denote the in-plane bond lengths parallel and perpendicular to the domain wall, while β is the average bond angle in the z direction. (a), (b) All values converge to bulk values with the exception of $\alpha_{\perp,90^\circ}$, which is why these have been omitted from the plot.

the Goodenough-Kanamori-Anderson rules, for d^3-d^3 cation configurations, the exchange is most antiferromagnetic at 180°, increasingly more ferromagnetic for intermediate angles approaching 150°, and fully ferromagnetic at 90° [68,69]. Octahedral distortions and deviating bond angles and lengths at ferroelastic domain walls can, as a result, stabilize a magnetic order different from the ground state found within bulk material. These are properties that are not captured through group-theoretical analysis or order-parameter profiles. The specific alterations of bond lengths and angles for each domain wall were therefore calculated as a function of the distance from the wall, shown in Fig. 3. It is evident that only the 90° wall has a component of angle narrowing (δ) and bond elongation (β) compatible with ferromagnetism, both in the z direction.

To test the susceptibility of the local octahedral environment toward different magnetic orders, a MW was imposed on top of the ferroelastic domain wall. It is noted that this collinear magnetic wall analysis follows the same procedure as Ref. [33], but considers both 90° and mirror-type domain walls, as well as the coupling between the polar distortion and every spin ordering. Each collinear magnetic wall is then confined to the two octahedral layers adjacent to the center of each twin wall. Delineating each possible magnetic order, through parallel or antiparallel spins along each bonding direction (x, y, and z), amounts to eight different magnetic walls. Half of them correspond to a finite analog of the regular bulk magnetic orders, and are therefore denoted, for example, "C-type" since they are not strictly three-dimensional; see Fig. 4(a). To evaluate the energetics of each magnetic wall, the formation energy was calculated according to the following relation:

$$\Delta E_{\mathrm{MW}} = \frac{1}{A_{DW}} \times \big[(E_{\mathrm{MW,DW}} - E_{\mathrm{MW,bulk}}) - (E_{\mathrm{G\text{-}AFM,DW}} - E_{\mathrm{G\text{-}AFM,bulk}}) \big], \tag{5}$$

where the latter term corresponds to the formation energy of each ferroelastic domain wall, $E_{f,\mathrm{DW}}$. This energy difference is a measure of the preference for a magnetic wall to reside within a twin wall compared to the bulk structure. It was ensured that the magnitude of the magnetic moments only showed small deviations from the bulk value of $2.8\,\mu_B$ for each Mn atom.

The resulting ΔE_{MW} for the four lowest energy magnetic walls along with the only magnetic wall with a net magnetic moment, FM-type, is presented in Fig. 4(b). For results concerning every wall type, see Sec. III A in the Supplemental Material [53]. In both the 90° and mirror domain walls, it is found that the C-type magnetic order leads to the largest energy lowering, with $\Delta E_{\text{C-type},90^\circ} = -6.85\,\mathrm{mJ/m^2}$ and $\Delta E_{\text{C-type, mirror}} = -1.78\,\mathrm{mJ/m^2}$. Accordingly, the local structure of both domain walls favors parallel spins in the out-of-plane direction and opposes parallel spins in the remaining xy plane. The second and third lowest formation energies result from the MW2 and MW3 configurations, which both also have parallel spins in the z direction, while the highest energy configurations are the A-type and FM magnetic walls.

From these results, the cost of parallel versus antiparallel spins in each direction can be inferred, seeing that the z direction parallel spins lead to the largest energy lowering, while a larger degree of spin alignment in the x and y directions leads to an energy gain. This can be understood in terms of the geometric considerations stated in the Goodenough-Kanamori formalism. As previously discussed, it is clear that for the 90° domain wall, the bond angles become smaller in the z direction while straightening in the x and y directions; see Fig. 3. For the less distorted mirror domain wall, all angles become larger at the wall but with an overall smaller deviation from bulk values than observed at the 90° domain wall. In terms of bond lengths, an inverted but similar trend is found. This correlates well with the more significant energy reduction for the C-type magnetic wall and with the larger overall variance in formation energies seen for the 90° domain wall. Although none of these magnetic walls give a lower energy than a fully G-AFM ground state, the energetic trends still demonstrate the propensity of the domain wall geometry toward a different magnetic ordering, implying a greatly locally enhanced magnetic susceptibility. For all the magnetic wall orderings, the same quantitative alterations in angle and bond deformation as seen in the bulk is observed at the domain walls.

Decomposing the magnetic order parameter in terms of the irreps of the *Pnma* space group, it is found that there are four sets of symmetry-allowed magnetic orders that also allow canting. However, none of these allow a magnetoelectric coupling because inversion symmetry is still conserved. This is also consistent with there being no third-order coupling allowed between the magnetic order and the octahedral tilting modes for B-site magnetism. The only way to activate a magnetoelectric response is therefore through inversion

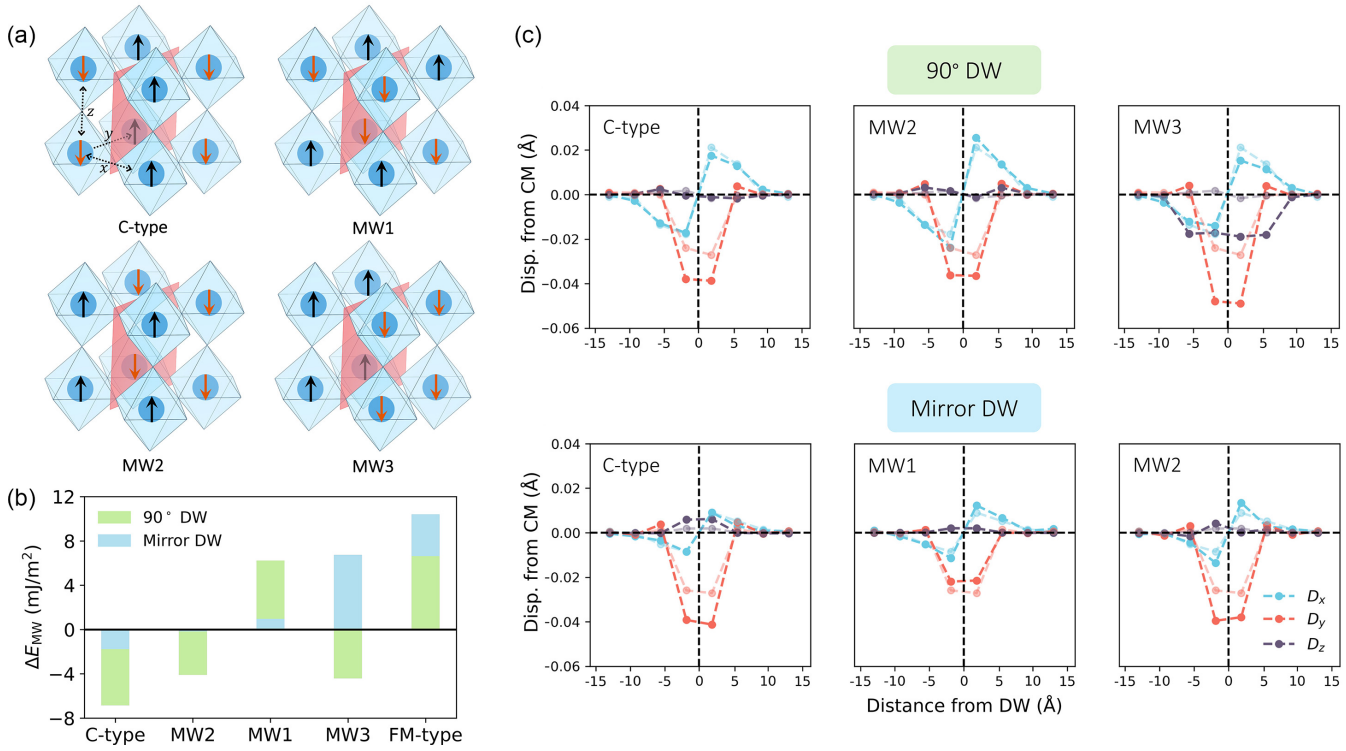


FIG. 4. (a) Spin orders for the four lowest energy magnetic wall (MW) configurations. The Cartesian axes coincide with those in Fig. 1. The position of the domain wall is indicated by the red plane. Black and red arrows represent spin up and spin down. (b) Formation energies from placing a magnetic wall at the domain wall as opposed to a bulk structure, for a selection of spin orders, sorted with respect to the mirror domain wall. (c) Polar distortion profiles for the lowest energy magnetic walls for each respective domain wall type. For each magnetic wall, the corresponding ground state distortion is shown at a higher transparency for comparison. The data is plotted without fits to hyperbolic functions to highlight the differences between the profiles.

symmetry breaking [27,31,70]. Calculating the displacement of Mn from the CM of each oxygen octahedra, we find that there is such an induced effect also in the twin walls of $CaMnO_3$; see Fig. 4(c).

For almost every magnetic wall, there is an enhancement of the polar distortion with the degree of spin alignment. Although the distortion profiles are qualitatively different between the two ferroelastic domain wall types, for every magnetic wall with parallel spins in the z direction, an enhancement of the net D_y polar distortion is observed both in the 90° and mirror domain wall. Particularly, for the MW3 wall, the polar distortion is almost twice as large. Some spin orders also break the antipolar or polar order of the displacements. For polar distortion profiles for each magnetic order, see Sec. III B in the Supplemental Material [53].

Although it is difficult to disentangle the exact coupling between these order parameters due to the nature of the symmetry breaking at the domain wall, it is evident that the emergence of a polar distortion lifts the restriction forbidding a magnetoelectric coupling. This is, however, not a direct coupling, but an indirect link through the primary order parameter.

3. Noncollinear magnetic calculations

In the preceding calculations, all spins were restricted to a collinear setting with no coupling to the lattice degrees of freedom. From previous work on $CaMnO_3$, it was shown that the ground state is a canted G-AFM order with a weak ferromagnetic component, specifically the $G_xA_yF_z$ spin configuration [27]. It is noted that this magnetic ordering is determined with respect to the primitive unit cell. The easy axis (G_x) is therefore in the $[1\bar{1}0]$ direction relative to the supercell coordinate axes and rotates by 45° across the domain wall. This also means that the net magnetization is in the direction found to exhibit the highest susceptibility toward a parallel spin configuration in a ferroelastic domain wall, as well as a notable coupling to the net polar displacement. It is therefore reasonable to anticipate a coupling between the canted antiferromagnetic ground state and the local symmetry at the twin wall, driving a larger degree of spin alignment such as observed in the collinear calculations. These effects are expected to be more prominent for the 90° domain wall as it exhibits the largest and most favorable distortions, which is why the analysis is limited to this wall type.

To determine the most stable spin orientation of a G-AFM ordering, bulk calculations were conducted, confirming the correct symmetry-allowed canting pattern for each crystallographic direction and that the ground state is $G_xA_yF_z$. Assuming that the easy axis is conserved within each domain, this magnetic ordering was imposed on a $6 \times 1 \times 1$ supercell with the converged wall geometry of the $8 \times 1 \times 1$ cell, so there is a 90° rotation of the spin direction at the domain wall. This allows two options where the spins at the interface

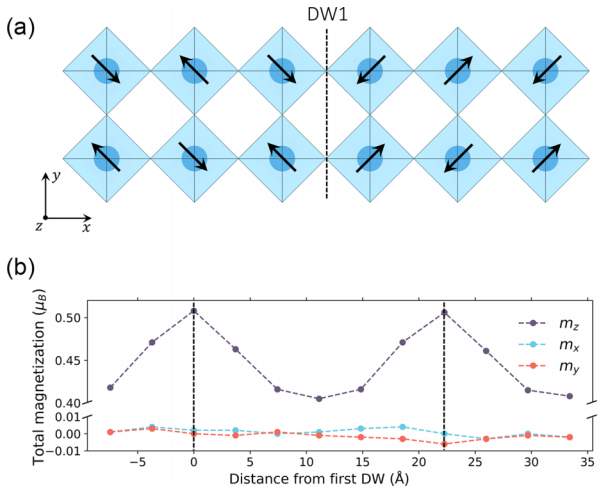


FIG. 5. (a) The initial magnetic order prior to the self-consistent spin rotation. The magnetic domain wall corresponds to a mirror symmetric interface (if the spins are not treated as axial vectors). (b) The resulting average magnetization of one unit cell consisting of eight Mn atoms. While m_x and m_y cancel each other, there is a net magnetization, m_z, in the out-of-plane direction. Note the break in the y-axis scale.

are either mirrored or rotated. The mirrored configuration was found to give the lowest energy by 0.01 meV/f u. and is illustrated in Fig. 5(a).

By optimizing spin directions while keeping atomic positions fixed, we observed an increase in the canting angle both in the xy plane from 1.5° to 2.3°, while in the z direction the canting angle only increased from 1.0° to 1.3°. See Sec. IV in the Supplemental Material [53] for an outline of the domain wall canting in terms of spherical coordinates (ϕ, θ). As a result, there is a net increase in the magnetization in the out-of-plane direction, while the in-plane magnetization still cancels to zero; see Fig. 5(b). This applies to both domain walls despite the reversal of the net polar distortion at each respective wall. The energy of a single magnetic domain is also lower in energy than the two separate domains, probably because the cost of the magnetic interface is higher than the magnetic anisotropy energy for a supercell.

Detection of the enhanced out-of-plane magnetization requires experimental techniques that can spatially resolve magnetic moments at domain wall dimensions below the Néel temperature (T_N). This could be accomplished through direct imaging techniques such as spin-polarized scanning tunneling microscopy [71], magnetic force microscopy [72], or scanning nitrogen-vacancy magnetometry [73]. Lorentz transmission electron microscopy could also be able to resolve ferromagnetic moments at a spatial resolution smaller than the width of a twin wall [74].

The spin canting is a result of a complex interaction between the magnetocrystalline anisotropy energy (single-ion anisotropy), the superexchange coupling, and DMI, which all can depend on the displacement of oxygen through octahedral rotations [75,76]. Such analysis becomes increasingly difficult with lower structural symmetry. However, it has been found that the amplitude of the canting generally depends on the ratio of the DMI and superexchange interaction, where a larger octahedral distortion involves a smaller J and a larger canting [77]. The $G_xA_yF_z$ magnetic order parameter can also be decomposed in bilinear free energy terms, resulting in relations $M_3^+ \propto G_xA_y$ and $R_4^+ \propto G_xF_z$ [31]. Both of these considerations imply that there is a larger canting associated with an increase in the Q_{R_x} and Q_{R_y} order parameters, as observed at the 90° domain wall. This is also in accordance with the largest D_y enhancement resulting from parallel spins in the out-of-plane direction, since these rotations have the strongest effect for in-plane rotation angles. Repeating these single-point calculations with an incrementally increased displacement of Mn did not lead to any larger spin canting at the wall, proving that the polar response to the magnetic order is contingent on the rotational degrees of freedom.

Thus, the inversion symmetry breaking at the domain wall allows for a magnetoelectric effect. However, this is a strain-mediated response where the magnetic order couples to the polarization through a magnetoelastic-flexoelectric relation. Such a coupling response through an octahedral distortion is also observed, for example, in bulk Ruddlesden-Popper $Ca_3Mn_2O_7$ [9,78]. $CaMnO_3$ offers an untraditional route toward this effect. In addition, the abundance of ferroelastic nonpolar antiferromagnets, e.g., rare earth chromites, manganites, and ferrites among just perovskites, suggest the existence of more ideal ferroelastic domain walls with respect to local ferromagnetism, improper polarization, and magnetoelectric coupling.

IV. CONCLUSION

Ferroelastic twin walls in orthorhombic $CaMnO_3$ are shown to host local polarization and magnetization couplings. Broken inversion symmetry from gradients in octahedral tilting induce domain wall-centered polarization, while the resulting DMI vectors enhance out-of-plane Mn magnetization that is confined to the wall. This coupling between the local polarization and weak ferromagnetism strongly support a strain-mediated magnetoelectric response at ferroelastic twin walls, and is achieved only through the octahedral distortions. Octahedral rotations cannot ordinarily break inversion symmetry in perovskites, meaning a magnetoelectric coupling in the bulk is symmetry forbidden, while it is allowed in the two-dimensional pseudosymmetry of a domain wall. This effect is dependent on the domain wall geometry and strongest for twin walls associated with the largest strain gradient.

These results should also be general for all *Pnma* structures, which is the most common space group among the broad family of perovskites. In addition, we propose that ferroelastic twin walls in other bulk centrosymmetric antiferromagnets can induce local polarization and magnetization. Our results suggest that large strain gradients at domain walls give the strongest effect, implying that good candidates have narrow domain walls and large distortions relative to high-symmetry aristotype phases. Such features are typically found in compounds with high ferroelastic Curie temperatures making, e.g., $LaFeO_3$ a prime candidate.

ACKNOWLEDGMENTS

The authors thank N. Spaldin, M. Fiebig, J. Schultheiß, S. F. Weber, and K. Eggestad for valuable insight and

helpful discussions. Financial support for this work was received from the Research Council of Norway through Project No. 302506. Computational resources were provided by UNINETT Sigma2 through Project No. NN9264K.

DATA AVAILABILITY

The data that support the findings of this article are openly available [49].

[1] M. Fiebig, T. Lottermoser, D. Meier, and M. Trassin, The evolution of multiferroics, Nat. Rev. Mater. **1**, 16046 (2016).

[2] N. A. Hill, Why are there so few magnetic ferroelectrics? J. Phys. Chem. B **104**, 6694 (2000).

[3] H. J. Xiang, P. S. Wang, M.-H. Whangbo, and X. G. Gong, Unified model of ferroelectricity induced by spin order, Phys. Rev. B **88**, 054404 (2013).

[4] S.-W. Cheong and M. Mostovoy, Multiferroics: A magnetic twist for ferroelectricity, Nat. Mater. **6**, 13 (2007).

[5] T. Aoyama, K. Yamauchi, A. Iyama, S. Picozzi, K. Shimizu, and T. Kimura, Giant spin-driven ferroelectric polarization in $TbMnO_3$ under high pressure, Nat. Commun. **5**, 4927 (2014).

[6] Y. Tokura and S. Seki, Multiferroics with spiral spin orders, Adv. Mater. **22**, 1554 (2010).

[7] C. Ederer and N. A. Spaldin, Weak ferromagnetism and magnetoelectric coupling in bismuth ferrite, Phys. Rev. B **71**, 060401(R) (2005).

[8] C. J. Fennie, Ferroelectrically induced weak ferromagnetism by design, Phys. Rev. Lett. **100**, 167203 (2008).

[9] N. A. Benedek and C. J. Fennie, Hybrid improper ferroelectricity: A mechanism for controllable polarization-magnetization coupling, Phys. Rev. Lett. **106**, 107204 (2011).

[10] I. Dzyaloshinsky, A thermodynamic theory of "weak" ferromagnetism of antiferromagnetics, J. Phys. Chem. Solids **4**, 241 (1958).

[11] T. Moriya, Anisotropic superexchange interaction and weak ferromagnetism, Phys. Rev. **120**, 91 (1960).

[12] A. Marthinsen, C. Faber, U. Aschauer, N. A. Spaldin, and S. M. Selbach, Coupling and competition between ferroelectricity, magnetism, strain, and oxygen vacancies in $AMnO_3$ perovskites, MRS Commun. **6**, 182 (2016).

[13] E. Dagotto and Y. Tokura, Strongly correlated electronic materials: Present and future, MRS Bull. **33**, 1037 (2008).

[14] K. Terakura, Magnetism, orbital ordering and lattice distortion in perovskite transition-metal oxides, Prog. Mater. Sci. **52**, 388 (2007).

[15] J. B. Goodenough, Perspective on engineering transition-metal oxides, Chem. Mater. **26**, 820 (2014).

[16] Y. Zhou, Z. Chen, Z. Wu, X. Shen, J. Wang, J. Zhang, and H. Sun, Hybrid improper ferroelectricity and magnetoelectric coupling in a two-dimensional perovskite oxide, Phys. Rev. B **103**, 224409 (2021).

[17] U. Dey, E. E. McCabe, J. Íñiguez González, and N. C. Bristowe, Prediction of room temperature electric field reversal of magnetization in the family of $A_4B_3O_9$ layered oxides, Phys. Rev. Lett. **134**, 136801 (2025).

[18] D. Meier and S. M. Selbach, Ferroelectric domain walls for nanotechnology, Nat. Rev. Mater. **7**, 157 (2022).

[19] E. A. Eliseev, A. N. Morozovska, Y. Gu, A. Y. Borisevich, L.-Q. Chen, V. Gopalan, and S. V. Kalinin, Conductivity of twin-domain-wall/surface junctions in ferroelastics: Interplay of deformation potential, octahedral rotations, improper ferroelectricity, and flexoelectric coupling, Phys. Rev. B **86**, 085416 (2012).

[20] A. N. Morozovska, E. A. Eliseev, M. D. Glinchuk, L.-Q. Chen, and V. Gopalan, Interfacial polarization and pyroelectricity in antiferrodistortive structures induced by a flexoelectric effect and rotostriction, Phys. Rev. B **85**, 094107 (2012).

[21] A. Schiaffino and M. Stengel, Macroscopic polarization from antiferrodistortive cycloids in ferroelastic $SrTiO_3$, Phys. Rev. Lett. **119**, 137601 (2017).

[22] K. M. Rabe, Theoretical investigations of epitaxial strain effects in ferroelectric oxide thin films and superlattices, Curr. Opin. Solid State Mater. Sci. **9**, 122 (2005).

[23] N. A. Benedek, A. T. Mulder, and C. J. Fennie, Polar octahedral rotations: A path to new multifunctional materials, J. Solid State Chem. **195**, 11 (2012).

[24] Q. Zhou and K. M. Rabe, Strain-induced hybrid improper ferroelectricity in simple perovskites from first principles, arXiv:1306.1839.

[25] U. Aschauer and N. A. Spaldin, Competition and cooperation between antiferrodistortive and ferroelectric instabilities in the model perovskite $SrTiO_3$, J. Phys.: Condens. Matter **26**, 122203 (2014).

[26] U. Aschauer and N. A. Spaldin, Interplay between strain, defect charge state, and functionality in complex oxides, Appl. Phys. Lett. **109**, 031901 (2016).

[27] E. Bousquet and N. Spaldin, Induced magnetoelectric response in *Pnma* perovskites, Phys. Rev. Lett. **107**, 197603 (2011).

[28] S. Rooj, S. Saxena, and N. Ganguli, Altermagnetism in the orthorhombic *Pnma* structure through group theory and DFT calculations, Phys. Rev. B **111**, 014434 (2025).

[29] E. Bousquet and A. Cano, Non-collinear magnetism in multiferroic perovskites, J. Phys.: Condens. Matter **28**, 123001 (2016).

[30] J. Hong, A. Stroppa, J. Íñiguez, S. Picozzi, and D. Vanderbilt, Spin-phonon coupling effects in transition-metal perovskites: A DFT $+U$ and hybrid-functional study, Phys. Rev. B **85**, 054417 (2012).

[31] D. D. Khalyavin, A. N. Salak, P. Manuel, N. M. Olekhnovich, A. V. Pushkarev, Y. V. Radysh, A. V. Fedorchenko, E. L. Fertman, V. A. Desnenko, and M. G. Ferreira, Antisymmetric exchange in La-substituted $BiFe_{0.5}Sc_{0.5}O_3$ system: Symmetry adapted distortion modes approach, Z. Kristallogr. Cryst. Mater. **230**, 767 (2015).

[32] H. J. Zhao and J. Íñiguez, Creating multiferroic and conductive domain walls in common ferroelastic compounds, npj Comput. Mater. **5**, 92 (2019).

[33] P. Barone, D. Di Sante, and S. Picozzi, Improper origin of polar displacements at $CaTiO_3$ and $CaMnO_3$ twin walls, Phys. Rev. B **89**, 144104 (2014).

[34] P. Zhou, S. Dong, H. Liu, C. Ma, Z. Yan, C. Zhong, and J.-M. Liu, Ferroelectricity driven magnetism at domain

walls in $LaAlO_3/PbTiO_3$ superlattices, Sci. Rep. **5**, 13052 (2015).
[35] M. Daraktchiev, G. Catalan, and J. F. Scott, Landau theory of domain wall magnetoelectricity, Phys. Rev. B **81**, 224118 (2010).
[36] Y. Geng, N. Lee, Y. Choi, S.-W. Cheong, and W. Wu, Collective magnetism at multiferroic vortex domain walls, Nano Lett. **12**, 6055 (2012).
[37] K. Geirhos, B. Gross, B. G. Szigeti, A. Mehlin, S. Philipp, J. S. White, R. Cubitt, S. Widmann, S. Ghara, P. Lunkenheimer, *et al.*, Macroscopic manifestation of domain-wall magnetism and magnetoelectric effect in a Néel-type skyrmion host, npj Quantum Mater. **5**, 44 (2020).
[38] S. Farokhipoor, C. Magén, S. Venkatesan, J. Íñiguez, C. J. Daumont, D. Rubi, E. Snoeck, M. Mostovoy, C. De Graaf, A. Müller, *et al.*, Artificial chemical and magnetic structure at the domain walls of an epitaxial oxide, Nature (London) **515**, 379 (2014).
[39] G. Kresse and J. Furthmüller, Efficient iterative schemes for *ab initio* total-energy calculations using a plane-wave basis set, Phys. Rev. B **54**, 11169 (1996).
[40] G. Kresse and D. Joubert, From ultrasoft pseudopotentials to the projector augmented-wave method, Phys. Rev. B **59**, 1758 (1999).
[41] J. P. Perdew, A. Ruzsinszky, G. I. Csonka, O. A. Vydrov, G. E. Scuseria, L. A. Constantin, X. Zhou, and K. Burke, Restoring the density-gradient expansion for exchange in solids and surfaces, Phys. Rev. Lett. **100**, 136406 (2008).
[42] S. L. Dudarev, G. A. Botton, S. Y. Savrasov, C. J. Humphreys, and A. P. Sutton, Electron-energy-loss spectra and the structural stability of nickel oxide: An LSDA+U study, Phys. Rev. B **57**, 1505 (1998).
[43] V. I. Anisimov, J. Zaanen, and O. K. Andersen, Band theory and Mott insulators: Hubbard U instead of Stoner I, Phys. Rev. B **44**, 943 (1991).
[44] P. E. Blöchl, Projector augmented-wave method, Phys. Rev. B **50**, 17953 (1994).
[45] A. Togo, First-principles phonon calculations with phonopy and phono3py, J. Phys. Soc. Jpn. **92**, 012001 (2023).
[46] A. Togo, L. Chaput, T. Tadano, and I. Tanaka, Implementation strategies in phonopy and phono3py, J. Phys.: Condens. Matter **35**, 353001 (2023).
[47] H. T. S. Stokes, D. M. Hatch, and B. J. Campbell, ISOTROPY software suite, iso.byu.edu.
[48] K. Momma and F. Izumi, *VESTA3* for three-dimensional visualization of crystal, volumetric and morphology data, J. Appl. Crystallogr. **44**, 1272 (2011).
[49] I. C. Skogvoll, B. A. D. Williamson, and S. M. Selbach, Structure files—ferroelastic domain walls in $CaMnO_3$, Zenodo 2025, https://doi.org/10.5281/zenodo.17637915.
[50] H. T. Stokes, E. H. Kisi, D. M. Hatch, and C. J. Howard, Group-theoretical analysis of octahedral tilting in ferroelectric perovskites, Acta Crystallogr. Sect. B **58**, 934 (2002).
[51] J. Klarbring and S. I. Simak, Nature of the octahedral tilting phase transitions in perovskites: A case study of $CaMnO_3$, Phys. Rev. B **97**, 024108 (2018).
[52] C.-J. Eklund, C. J. Fennie, and K. M. Rabe, Strain-induced ferroelectricity in orthorhombic $CaTiO_3$ from first principles, Phys. Rev. B **79**, 220101(R) (2009).
[53] See Supplemental Material at http://link.aps.org/supplemental/10.1103/6y99-279q for more details on the improper mechanism coupling rotational and antipolar modes, the domain wall geometry, and the local magnetic order, which includes Figs. S1 -S6 and Ref. [54].
[54] N. A. Benedek and M. A. Hayward, Hybrid improper ferroelectricity: A theoretical, computational, and synthetic perspective, Annu. Rev. Mater. Res. **52**, 331 (2022).
[55] Z. Zanolli, J. C. Wojdeł, J. Íñiguez, and P. Ghosez, Electric control of the magnetization in $BiFeO_3/LaFeO_3$ superlattices, Phys. Rev. B **88**, 060102(R) (2013).
[56] Y. S. Oh, X. Luo, F.-T. Huang, Y. Wang, and S.-W. Cheong, Experimental demonstration of hybrid improper ferroelectricity and the presence of abundant charged walls in $(Ca, Sr)_3Ti_2O_7$ crystals, Nat. Mater. **14**, 407 (2015).
[57] F.-T. Huang, F. Xue, B. Gao, L. Wang, X. Luo, W. Cai, X.-Z. Lu, J. Rondinelli, L. Chen, and S.-W. Cheong, Domain topology and domain switching kinetics in a hybrid improper ferroelectric, Nat. Commun. **7**, 11602 (2016).
[58] M. Calleja, M. T. Dove, and E. K. Salje, Trapping of oxygen vacancies on twin walls of $CaTiO_3$: A computer simulation study, J. Phys.: Condens. Matter **15**, 2301 (2003).
[59] X.-K. Wei, A. K. Tagantsev, A. Kvasov, K. Roleder, C.-L. Jia, and N. Setter, Ferroelectric translational antiphase boundaries in nonpolar materials, Nat. Commun. **5**, 3031 (2014).
[60] X. Zhang, B. Wang, Y. Ji, F. Xue, Y. Wang, L.-Q. Chen, and C.-W. Nan, First-principles calculations of domain wall energies of prototypical ferroelectric perovskites, Acta Mater. **242**, 118351 (2023).
[61] K. Eggestad, B. A. D. Williamson, D. Meier, and S. M. Selbach, Mobile intrinsic point defects for conductive neutral domain walls in $LiNbO_3$, J. Mater. Chem. C **12**, 17099 (2024).
[62] E. Salje, *Phase Transitions in Ferroelastic and Co-Elastic Crystals* (Cambridge University Press, Cambridge, 1990).
[63] G. Lu and E. K. Salje, Temperature dependence of emerging properties of ferroelastic domain walls in $CaTiO_3$, J. Appl. Phys. **137**, 154102 (2025).
[64] P. W. Anderson, Antiferromagnetism. Theory of superexchange interaction, Phys. Rev. **79**, 350 (1950).
[65] J. Kanamori, Superexchange interaction and symmetry properties of electron orbitals, J. Phys. Chem. Solids **10**, 87 (1959).
[66] P. W. Anderson, New approach to the theory of superexchange interactions, Phys. Rev. **115**, 2 (1959).
[67] H. Tsukahara, S. Ishibashi, and K. Terakura, First-principles calculations for the magnetic phase diagram in electron-doped $CaMnO_3$ under compressive and tensile strains, Phys. Rev. B **81**, 214108 (2010).
[68] J. B. Goodenough, *Magnetism and the Chemical Bond* (John Wiley & Sons, New York, 1963).
[69] J. N. Lalena and D. A. Cleary, *Principles of Inorganic Materials Design* (John Wiley & Sons, New York, 2005).
[70] M. S. Senn and N. C. Bristowe, A group-theoretical approach to enumerating magnetoelectric and multiferroic couplings in perovskites, Acta Crystallogr. Sect. A **74**, 308 (2018).
[71] S.-W. Cheong, M. Fiebig, W. Wu, L. Chapon, and V. Kiryukhin, Seeing is believing: Visualization of antiferromagnetic domains, npj Quantum Mater. **5**, 3 (2020).

[72] Y. Geng, H. Das, A. L. Wysocki, X. Wang, S. Cheong, M. Mostovoy, C. J. Fennie, and W. Wu, Direct visualization of magnetoelectric domains, Nat. Mater. **13**, 163 (2014).

[73] J.-Y. Chauleau, T. Chirac, S. Fusil, V. Garcia, W. Akhtar, J. Tranchida, P. Thibaudeau, I. Gross, C. Blouzon, A. Finco, *et al.*, Electric and antiferromagnetic chiral textures at multiferroic domain walls, Nat. Mater. **19**, 386 (2020).

[74] M.-G. Han, J. A. Garlow, Y. Liu, H. Zhang, J. Li, D. DiMarzio, M. W. Knight, C. Petrovic, D. Jariwala, and Y. Zhu, Topological magnetic-spin textures in two-dimensional van der Waals $Cr_2Ge_2Te_6$, Nano Lett. **19**, 7859 (2019).

[75] J.-S. Zhou, L. G. Marshall, Z.-Y. Li, X. Li, and J.-M. He, Weak ferromagnetism in perovskite oxides, Phys. Rev. B **102**, 104420 (2020).

[76] I. A. Sergienko and E. Dagotto, Role of the Dzyaloshinskii-Moriya interaction in multiferroic perovskites, Phys. Rev. B **73**, 094434 (2006).

[77] C. Weingart, N. Spaldin, and E. Bousquet, Noncollinear magnetism and single-ion anisotropy in multiferroic perovskites, Phys. Rev. B **86**, 094413 (2012).

[78] Y. Zemp, M. Trassin, E. Gradauskaite, B. Gao, S.-W. Cheong, T. Lottermoser, M. Fiebig, and M. C. Weber, Magnetoelectric coupling in the multiferroic hybrid-improper ferroelectric $Ca_3Mn_{1.9}Ti_{0.1}O7$, Phys. Rev. B **109**, 184417 (2024).